*Article*

# Heterojunction Engineering of All-Inorganic $CsPbI_3$ Perovskite for High-Responsivity SWIR Photodetectors Performed at Room Temperature

Sydney Schmidt [1,†], Haley Fisher [1,†], Xia Li [1], Jesse B. Brown [1], Yuqin Qian [1], Van Malmquist [1], Avetik Harutyunyan [2], Gugang Chen [2,*], and Yi Rao [1,*]

[1] Department of Chemistry and Biochemistry, Utah State University, Logan, UT 84322, USA
[2] Honda Research Institute, USA Inc., San Jose, CA 95134, USA
* Correspondence: gchen@honda-ri.com (G.C.); yi.rao@usu.edu (Y.R.)
† These authors contributed equally to this work.
Received: 20 April 2025; Revised: 10 July 2025; Accepted: 12 July 2025; Published: 30 July 2025

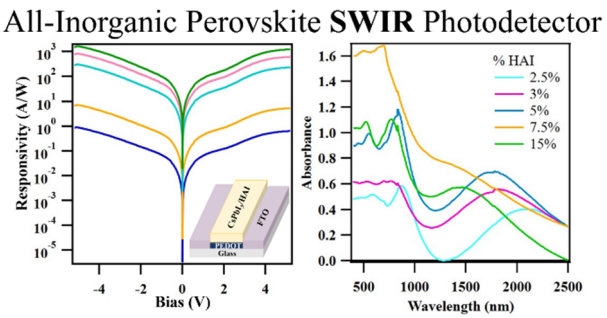


**Abstract:** Short-wave infrared (SWIR) light, 0.9–2.5 μm wavelengths, has widespread applications, including inspection processes, nighttime imaging, and machine vision. As such, there is increasing demand for practical and effective SWIR detectors. Many current SWIR photodetectors are based on high-cost materials and require cryogenic cooling. Perovskite materials, including $CsPbI_3$, have been effectively used as photodetectors in the UV to near IR ranges, but their large bandgaps limit their use for lower energy SWIR light. In this report we introduce an all-inorganic perovskite photodetector based on $CsPbI_3$ with heterojunction engineering for efficient and practical detection in the SWIR range at room temperature. The devices undergo a simple, solution-based fabrication process which includes spin-coating under ambient conditions and moderate annealing temperatures. Without additional cooling, the SWIR devices produce excellent results at room temperature with responsivity of $1.65 \times 10^3$ A $W^{-1}$ and a specific detectivity of $8.0 \times 10^{10}$ Jones under 0.28 mW $cm^{-2}$ of 1310 nm light and bias of −5 V. This material shows not only high response but also high sensitivity, making it stand out in the field of SWIR photodetection with the additional benefits of low-cost production and room temperature operation.

**Keywords:** perovskite; short-wave IR photodetectors; Hetero-junction

## 1. Introduction

Short-wave infrared (SWIR) light, 0.9–2.5 μm wavelengths, has become important in many applications, such as remote sensing, communications, spectroscopy, security, and hyperspectral imaging processes [1–5]. In the communications sector, utilization of SWIR wavelengths enables free-space optical communication systems and optical wireless communications where radio frequencies are congested [6]. SWIR imaging is able to penetrate harsh weather conditions like fog better than visible light, providing usefulness in automotive applications [1,7]. Furthermore, SWIR sensors can reliably distinguish between components in the recycling process of lithium-ion batteries, increasing recycling efficiency and decreasing waste [8]. Sensors for this wavelength range have also been applied in very-high resolution satellite imaging, making possible large-scale vegetation mapping for conservation and forest management [9]. Additionally, machine vision in the SWIR is important in military applications for the identification of camouflaged materials and even the detection of landmines and chemical warfare agents [2,10]. As such, practical, affordable, and sensitive SWIR photodetectors are needed.

Current state-of-the art SWIR photodetectors are made from mixed-alloy semiconductors such InGaAs, due to their favorable sensitivities in the range of $10^3$ A $W^{-1}$ at 1550 nm with specific detectivity on the order of $10^{12}$ Jones [1,11–13]. However, such materials are economically and energetically expensive, often operating under

cryogenic conditions to achieve optimum results, warranting the search for new SWIR detection materials [5]. An emerging candidate for SWIR applications is colloidal quantum dot detectors, due to their tunable spectral properties, solution-processability, silicon-compatible fabrication, and low cost [10,13–15]. Lead-based quantum dots (PbS and PbSe QDs) are one of the most promising materials, having solution-processibility, being low-cost to produce, and possessing tunable bandgaps within the infrared [16]. In 2021, Kwon, et al. fabricated a solution-processed SWIR detector based on PbS QDs using conductive polymer [17]. The material had an absorption maximum at 1410 nm and achieved an ultra-high responsivity of 6 kA $W^{-1}$ [15]. Chen et al. used a layer-by-layer spray technique to form a well-rounded PbS QD photodetector with a responsivity over 360 A $W^{-1}$ under 1250 nm light, also yielding a detectivity on the scale of $10^{12}$ Jones [18]. Yet, these materials have quantum efficiency and charge transport that are low compared to epitaxial InGaAs, HgCdTe, or InSb detectors [14,15,19]. On the other hand, graphene-based technologies possess many attractive qualities as SWIR detectors [10,13–15]. Due its near-zero bandgap, graphene exhibits broadband absorption into the far infrared with fast response and high carrier mobility [1,20–22] However, graphene has very low light absorption of about 2.3% which limits its responsivity to the mA $W^{-1}$ scale [1,13,20]. Recently, another promising candidate has emerged in the field of SWIR detection: perovskites materials [23–26]. Known for having good optoelectronic properties and simple synthesis, these materials are finding expanded applications in photodetection [23,27–30].

Perovskites are designer materials which have received enormous attention in recent years in fields spanning from catalysis to solar cells with unprecedented performance [23,31,32]. These materials take the general form $ABX_3$, where A is a cation such as methylammonium, B is a transition metal such as lead, and X is a halogen anion; all together it possess the same type of crystal structure as $CaTiO_3$ [23]. Perovskite photodetectors (PPDs) exhibit notable characteristics including a tunable bandgap, high carrier mobility, and solution-based coating processes which make them appealing for commercialization [28,33]. Organic-inorganic PDDs, notably methylammonium lead triiodide ($MAPbI_3$) PDDs have repeatedly shown useful response in the UV to near-IR (about 300–800 nm) regions but with highly variable responsivity, specific detectivity, and external quantum efficiency (EQE) [28,34,35]. However, the wide bandgap of these perovskite materials limits their performance in longer wavelengths, such as SWIR [28,36]. Additionally, organic-inorganic hybrid PPDs suffer from instability in oxygen and moisture, making broader application difficult [28]. Recent research from our group introduced a hydrazinium-doped methylammonium lead iodide perovskite, $[(MAI)_{1-x}(HAI)_x]_2[PbI_2]$, a mixed halide perovskite as a powerful SWIR-absorbing material, whose peak absorption was tunable based on the proportion of MAI to HAI [26]. The PPD made using this material demonstrated a broad detection range, responsivity of over $10^2$ A $W^{-1}$ at 1310 nm, good specific detectivity and high external quantum efficiency: all at ambient temperature and pressure. While this novel material showed superior stability over pure $MAPbI_3$, its relative photocurrent decreased to about 20% of its original value after 8 months [26].

Research into the application of more stable all-inorganic perovskites as photodetectors is an active field. All-inorganic lead halide perovskites offer superior stability by replacing the MA group with Cs [37]. Cs-based inorganic PDDs have shown high temperature tolerance, even maintaining 70% visible photodetection ability under 373 K heat after 9 h, showing promise for real-world use. However, this photodetector was essentially blind to wavelengths greater than 430 nm [38]. In 2021, Pintor Monroy et al. published an all-inorganic, all-evaporated $CsPbI_3$ photodetector with NiO and $TiO_2$ for broad-band use within the visible range. They formed a fast-responding mixed-phase $CsPbI_3$ to obtain a desirable bandgap of 1.7 eV with responsivity of 0.4 A $W^{-1}$, detectivity of over $10^{12}$ Jones, and EQE greater than 70% [39]. $CsPbBr_3$, having a bandgap of 2.3 eV, is another popular inorganic perovskite for photodetection. For example, Liu et al. fabricated a self-powered, evaporated $CsPbBr_3$ PPD without charge transport layers with the simple configuration ITO/$CsPbBr_3$/Ag [40]. The stability of this device was outstanding, along with responsivity 0.05 A $W^{-1}$ and specific detectivity near$10^{10}$ Jones for visible detection. Nevertheless, modifications to the perovskite must be made to decrease the bandgap and expand their usefulness to the SWIR regime.

To overcome the shortcomings of an all-inorganic $CsPbI_3$ PPD, we present here a unique preparation process by introducing hydrazinium iodide ($[NH_2NH_3^+\ I^-]$, HAI) stabilized by hydriodic acid (HI) for photodetection in the SWIR range based on the heterojunction approach of our recent organic-inorganic PPD []. With its facile synthesis and ambient-condition coating process, we developed an effective SWIR photodetector. The device achieved remarkably high responsivity and external quantum efficiency measured at room temperature.

## 2. Experimental Methods

### *2.1. Preparation of SWIR Materials*

For the SWIR material, $PbI_2$ (Sigma Aldrich, St. Louis, MO, USA, 99.995%), CsI (Alfa Aesar, Ward Hill, MA, USA, 99.9%), HAI (synthesized in-house) [26], DMF (Sigma Aldrich, St. Louis, MO, USA, anhydrous 99.8%), DMSO (Sigma Alrich, St. Louis, MO, USA, anhydrous ≥99.9%), GBL (Aldrich, St. Louis, MO, USA, ≥99%), and HI (Alfa Aesar, Ward Hill, MA, USA, 57% *w/w* aqueous solution stabilized with 1.5% hypophosphorus acid) were used. The solution was prepared in a 2:1 of CsI/HAI and $PbI_2$ ratio using CsI/HAI with 15% HAI, and $PbI_2$. The solvent used was a mixture of DMF, DMSO, and GBL. The solution was heated while stirring for 60–120 min producing a bright yellow solution. HI was added to the vial 3–10 min before coating and returned to heat. As a result, the sample solution color deepened to a rust red. After heating the substrates to 180–200 °C, 150 µL of the rust red $CsPbI_3$ sample solution was deposited and spin coated for 30–60 s.

### *2.2. Fabrication of SWIR Devices*

50 µm FTO-striped glass substrates were cleaned using Piranha solution (3:1 of $H_2SO_4$ and $H_2O_2$) before rinsing thoroughly and being stored in ethanol. Substrates were dried under an air stream and cleaned in an Ossila UV-ozone cleaner. Meanwhile, PEDOT:PSS (Heraeus) solution was sonicated for at least 30 min. 150 µL of PEDOT:PSS was deposited onto the substrate and spin-coated for 20–45 s. The substrates were then annealed at 145 °C under vacuum, then cooled to room temperature. After heating the substrates to 180–200 °C, the rust red $CsPbI_3$ sample solution was deposited on the PEDOT-coated device and spin coated for 30–60 s which resulted in a black coating. The device was then annealed at 100–130 °C for 20–50 min under vacuum which cooled to a pale-yellow color. This process is depicted in Figure S1.

### *2.3. Testing of SWIR Devices Performance*

The fabricated devices were prepared for testing by scraping off excess sample from the surface, leaving a stripe of perovskite over all active cells of the substrate. The testing was performed under ambient conditions in the dark inside a dehumidified shielding box to decrease environmental effects or disturbances. The light source was a 1310 nm laser (LPSC-1310-FC, Thorlabs, Newton, NJ, USA) with a $7.1 \times 10^{-2}$ $cm^2$ spot size and a Keithley 2401 source meter provided bias to the system and recorded current outputs. The laser output power was measured at 40.0 mW and regulated by an ND filter to desired levels. The light intensity was measured with a Newport 1916-R Optical Power Meter (Newport, Irvine, CA, USA).

### *2.4. Characterization of SWIR Materials and Devices*

Mott Schottky measurements were performed using a Gamry Instruments potentiostat from −1 V to 1 V with an AC voltage of 10 mV and frequency of 100 Hz. Electrochemical impedance spectroscopy (EIS) was performed from 10 kHz to 2 Hz using an AC voltage of 10 mV. Transient absorption (TA) spectroscopy was performed following the procedure of Han et al. (2020) [41]. Fluorescence lifetime measurements were performing using a 515 nm light source by doubling a fundamental light from a Carbide laser (Light Conversion, Vilnius, Lithuania) and detected by a time-correlated single photon counter (PicoQuant Gmbh, Berlin, Germany).

## 3. Results & Discussion

We begin our analysis of the all-inorganic $CsPbI_3$ material by determining its light absorption properties. Figure 1A shows absorption spectra of the material coated at a substrate temperature of 185 °C with varied amounts of HAI included, further explanation for calculating the percentage of HAI is in the SI. Depending on the composition, each spectrum shows a broad SWIR peak 1200–2500 nm, in addition to a peak at ca. 800 nm due to the classical perovskite semiconducting material. As the HAI content increases, the SWIR peak is blue-shifted. Additionally, scanning electron microscopy (SEM) images were also taken to analyze the surface morphology of the PPDs. The SEM image in Figure 1B shows the surface of the perovskite film at 1000× magnification, demonstrating that the film was compact. In general, the images were found to be relatively homogenous but with very small holes. It also shows some self-assembled tree-branch like structures. Careful inspection of the SEM image shows topographical changes in the sample, with most of the material being spread out in florets with thicker structures being more disperse. Further optimization of the coating process may resolve the small holes and structural heterogeneity and potentially improve device performance. Figure S2 shows the XRD spectrum of our prepared $CsPbI_3$ material with HI. In comparison, Haque

et al. demonstrates that even with varied amounts of HI, the α-$CsPbI_3$ diffraction peaks which result from the 100, 110, 200, 211 and 220 Miller indices occur at approximate 2θ values of 14, 21, 28, 36 and 42, respectively. As our sample solution contains 40 μL of HI per mL of solution, it was expected that its XRD spectrum should be similar to the literature. Our spectrum contains some corresponding peaks near 21, 28, and 36, yet lacks other characteristic peaks and contains many additional peaks, making the spectrum difficult to decipher. Our XRD results are more similar–but not a perfect match– to that of δ-$CsPbI_3$ shown by Montecucco et al., with many more peaks visible including those caused by FTO. This may indicate that our compound has characteristics of both δ and non-δ $CsPbI_3$, and that the inclusion of HAI greatly affects crystal formation in the sample and warrants further investigation [3,37,42–45]. Counterintuitively, our PPD utilizes the δ phase of $CsPbI_3$ for detection of longer wavelengths than the aforementioned visible detectors, without the need for strict environmental controls. This generally undesirable form's bandgap is considered too large for visible detectors but has been reduced to accommodate SWIR wavelengths with the inclusion of HAI.

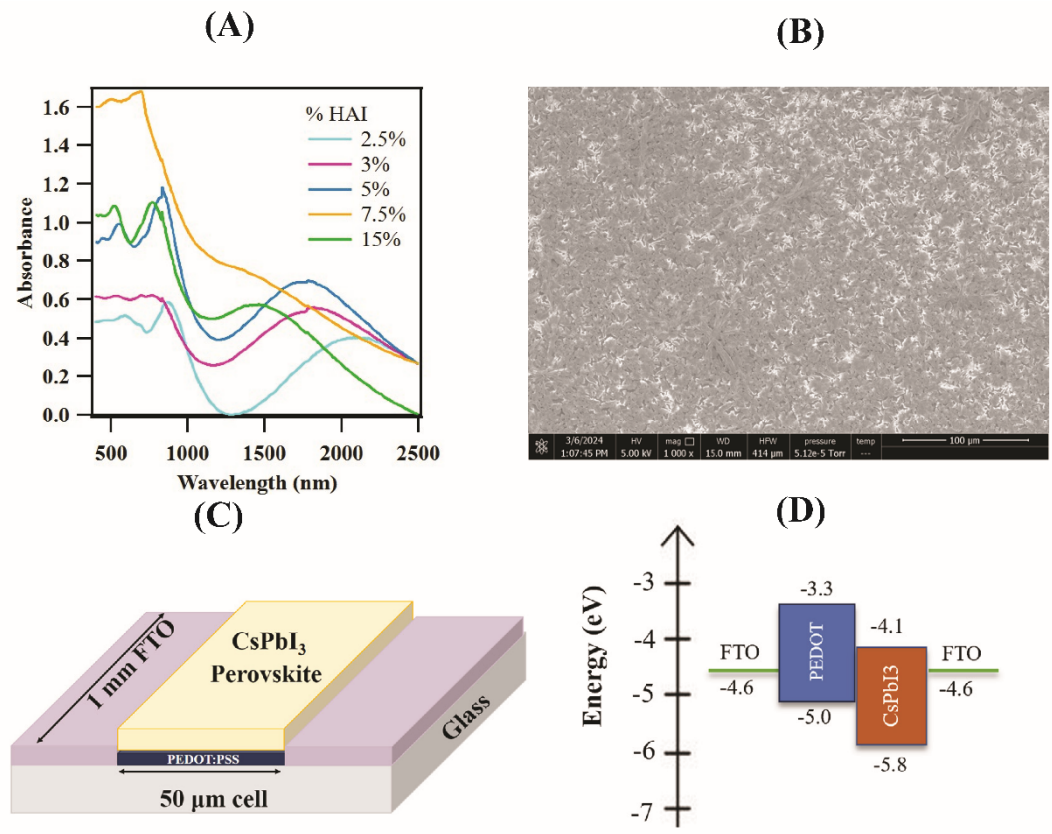


**Figure 1.** (**A**) Absorption spectra of $CsPbI_3$ material with different percentages of HAI. (**B**) SEM image of the perovskite surface; (**C**) Schematic of $CsPbI_3$ photodetector on FTO glass; (**D**) Energy level diagram of the perovskite photodetector.

After establishing the absorptive properties of the $CsPbI_3$ material, we turned to a simple device fabrication strategy. The as-prepared all-inorganic perovskite photodetectors consist of FTO-striped glass coated with $5 \times 10^{-4}$ $cm^2$ layers of PEDOT:PSS and $CsPbI_3$ in the center, with FTO on either side of this stripe as shown in Figure 1C. The resulting matchup of electronic band structures using pure $CsPbI_3$ as the perovskite is shown in Figure 1D. $CsPbI_3$ has a valence band (VB) at −5.8 eV and a conduction band (CB) at −4.1 eV resulting in a bandgap of 1.7 eV [5]. Additionally, the PEDOT:PSS HTL has a bandgap of 1.7 eV as well, with the work function of commercial FTO at −4.6 eV [46,47]. The absorption spectrum of our PPD is shown in Figure S3. A local absorption peak occurs at 725 nm, corresponding to the bandgap energy of $CsPbI_3$. Interestingly, the absorption maximum for the fabricated $CsPbI_3$ device occurs at 1132 nm (1.095 eV), suggesting that notable heterojunction or intraband absorption are occurring in our HAI-doped material [15,35].

Several metrics are used to analyze the performance of photodetector devices. The first is the responsivity, *R* (A $W^{-1}$), which represents the ability of a photodetector to convert incoming light into useful electrical signals. Responsivity is the ratio of output current to incident light power on the active area:

$$R = \frac{I_p - I_d}{A * P} \quad (1)$$

where $I_p$ is the photocurrent (A), $I_d$ is the dark current (A), $A$ is the cell area ($cm^2$), and $P$ is the incident light fluence (W $cm^{-2}$). Additionally, the calculations for the incident light fluence are also found in the Supplementary Materials. As shown in Figure 2A, we measured the responsivity of the PPD using a 1310 nm laser with incident fluence values from 0.28 to 567 mW $cm^{-2}$. We observed an impressive responsivity of $1.65 \times 10^3$ A $W^{-1}$ under 0.283 mW $cm^{-2}$ fluence at a bias of −5 V, indicating exceptional detection even at low levels of illumination. Under the same intensity at a bias of −1 V, the responsivity still reached a value of $1.01 \times 10^2$ A $W^{-1}$. Overall, low fluence achieved the highest responsivities and higher fluence maintained similar response curves at lower magnitudes. We can also look at the responsivity of our device as a function of incident fluence at different applied potentials, as shown in Figure 2B. At negative potentials, the responsivity of the all-inorganic PPD decreases quickly with increased fluence and is greater for larger magnitude applied negative bias. The net photocurrent, $I_p - I_d$, remains approximately constant, such that increases in responsivity are a function of the fluence. Assuming the resistance of our material is constant, Ohm's law explains the linearity of Figure 2B.

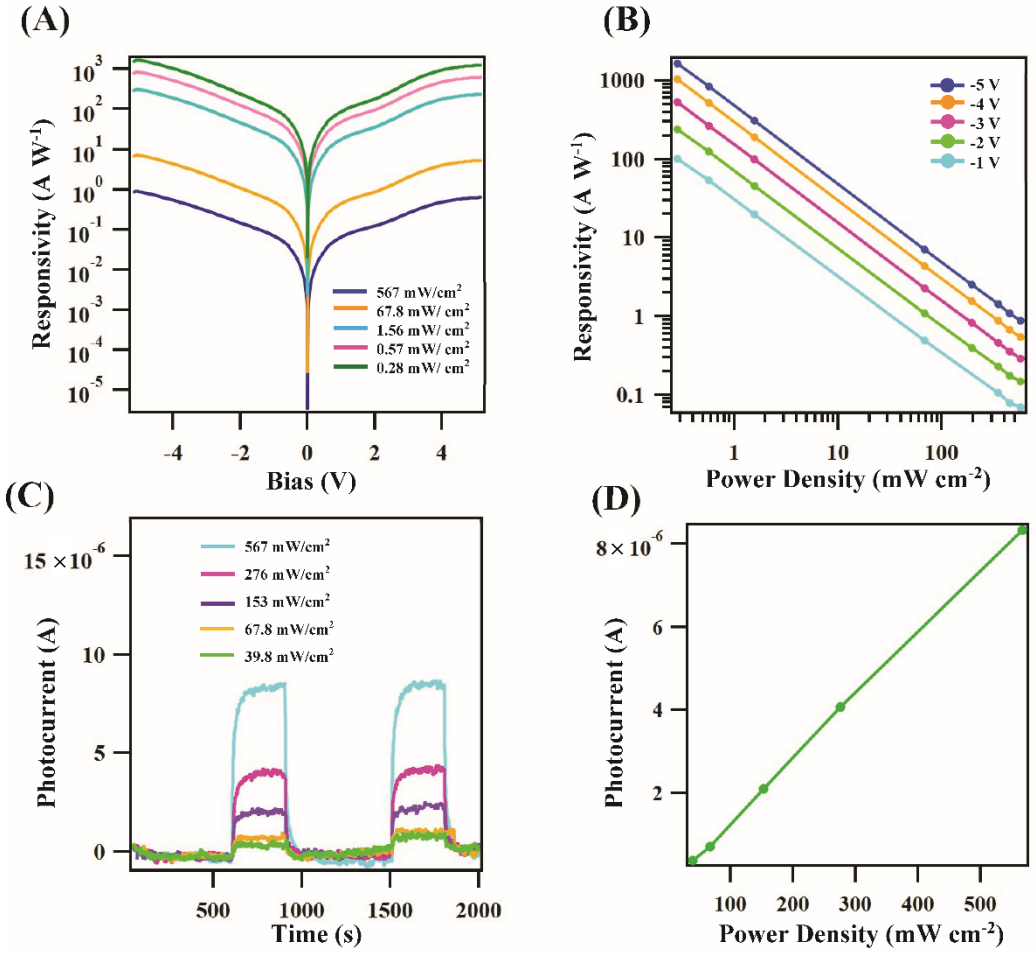


**Figure 2.** (**A**) Representative photoresponsivity curves at various power levels of 1310 nm illumination. (**B**) Responsivity at biases from −1 V to −5 V as a function of incident fluence. (**C**) Photocurrent through the device with 1310 nm light on and off under a bias of 3 V. (**D**) Photocurrent as a function of incident fluence.

Another important metric for photodetectors is their external quantum efficiency (EQE), which quantifies the number of free charge carriers generated from the photosensitive material per incident photon:

$$EQE = \frac{R * hc}{e\lambda} \quad (2)$$

Here, $h$ is Planck's constant ($6.626 \times 10^{-34}$ J s), $c$ is the speed of light ($3 \times 10^8$ m $s^{-1}$), and $e$ is the charge of a single electron ($1.602 \times 10^{-19}$ C). Using $R = 1.65 \times 10^3$ A $W^{-1}$ achieved under 0.283 mW/$cm^2$ and −5 V bias, the $EQE$ is found to be $1.48 \times 10^3$. Even at −1 V, the $EQE$ is 90.7.

Next, we investigated the generated photocurrent over time at different incident intensities, as shown in Figure 2C. An increase in photocurrent is observed when the sample is irradiated with 1310 nm laser light and quickly decreases to baseline when the light is blocked. It is also apparent that the photocurrent increases with incident fluence, and the detector's response is reproducible for multiple cycles. These experiments produced a net photocurrent ($I_p$–$I_d$) up to 8.8 μA at an incident fluence of 567 mW cm$^{-2}$. Furthermore, we observed a linear relationship between maximum photocurrent and applied fluence, as shown in Figure 2D. This is important when implementing the photodetector to easily scale the response with incident light intensity. The theoretical photoconductive gain, *G*, is a key parameter for evaluating the efficacy of a photodetector, representing the ratio of photogenerated charge carriers to absorbed incident photons in the material:

$$G = \frac{I_p h\nu}{ePA} \tag{3}$$

Here, *v* is the frequency of the incident photon (Hz). Under a bias of −5.0 V and intensity of 0.283 mW cm$^{-2}$, the gain was found to be 1.43 × 10$^3$. Even under only −1.0 V bias, the gain is 87.08, as shown in Table S1.

Specific detectivity, *D** (Jones), is a measure of sensitivity which quantifies the ability of the photodetector to discern weak light signals from noise, and can be computed as

$$D^* = \frac{\sqrt{A\Delta f}R}{i_n} = \frac{\sqrt{A\Delta f}}{NEP} \tag{4}$$

In this equation, Δ*f* is the bandwidth (Hz), $i_n$ is rms noise, *A* is the active area of detectors, and *NEP* denotes the noise equivalent power, or the amount of input signal required for the signal-to-noise ratio to be one [48]. Using the measurements shown in Figure S4, the specific detectivity of our device was found to be on the order of 8.0 × 10$^{10}$ Jones under a bias from −1.0 V to −5.0 V. Specific detectivity at other biases can be found in Table S2. With these baseline metrics of the all-inorganic PPD outlined, we can perform further analyses to better understand its mechanism for excellent performance.

First, Mott-Schottky measurements were used to characterize the SWIR materials. In such an analysis, the inverse of the square of the material's measured capacitance is plotted as a function of applied bias potential. A positive slope is characteristic of an *n*-type material while a negative slope indicates a *p*-type material [49]. Figure 3A shows an inverted "V" shape, where a positive slope occurs from −1.0 to 0 V and a negative slope occurs from 0 to 1 V. This indicates that a *p*-*n* junction was formed within the perovskite material due to the HAI doping process, since $CsPbI_3$ is an inherent *p*-type semiconductor. Next, fluorescence lifetime measurements were used to investigate the lifetime of photoinduced carriers to better understand the nature of the SWIR materials. The free carrier decay can be seen in Figure 3B, after a sharp increase in free carriers is caused by a 515 nm excitation pulse. A double exponential curve fitting was performed, yielding both fast ($\tau_1$) and slow ($\tau_2$) decay constants to be 10.7 ± 0.1 ns and 68.2 ± 0.7 ns, respectively, with an average ($\tau_{avg}$) of 39.5 ± 0.4 ns [50]. While there is variation in the carrier lifetime of $CsPbI_3$, these are comparable to other studies finding values between 33 and 50 ns [51–53]. These results suggest that the formed doped structures still have similar carrier lifetimes to $CsPbI_3$, allowing ample time for carrier extraction.

Last, to better understand how charge carriers flow in the heterojunction structure, transient absorption (TA) measurements were also conducted on the all-inorganic PPD. Figure 3C shows several representative TA spectra at delay times of −1, 0, 1, 10 and 100 ps between the 515 nm pump and the white light probe. A full 2D plot of this data including longer delay times is shown in Figure S5. The negative feature denotes photoinduced absorption (PIA) and is most clearly seen from 800 to 1000 nm with a shoulder at 1070 mm which decreases significantly with increasing delay as the excited state population declines. The time trace of the PIA at 1070 nm was extracted and fitted using a double exponential function, as shown in Figure 3D. The fitting yielded two fast decay time constants of 4.0 ± 0.3 ps and 25.9 ± 0.9 ps at 1070 nm, which may be due to forward and reverse charge transfer processes, respectively. These fast processes describe the processes by which the photogenerated carriers transfer between the doped and undoped perovskite.

As shown in Table 1, our heterojunction-engineered material produces SWIR responsivities far greater than other modern materials such as other perovskites [26], traditional semiconductors [54], hybrid materials [7,55], and quantum-confined systems [56] which operate at or below room temperature. Interestingly, a graphene/black phosphorus detector [57] has achieved responsivity on the same order as ours but requires meticulous fabrication where our PPD has the advantage of solution processibility and simple spin-coating fabrication.

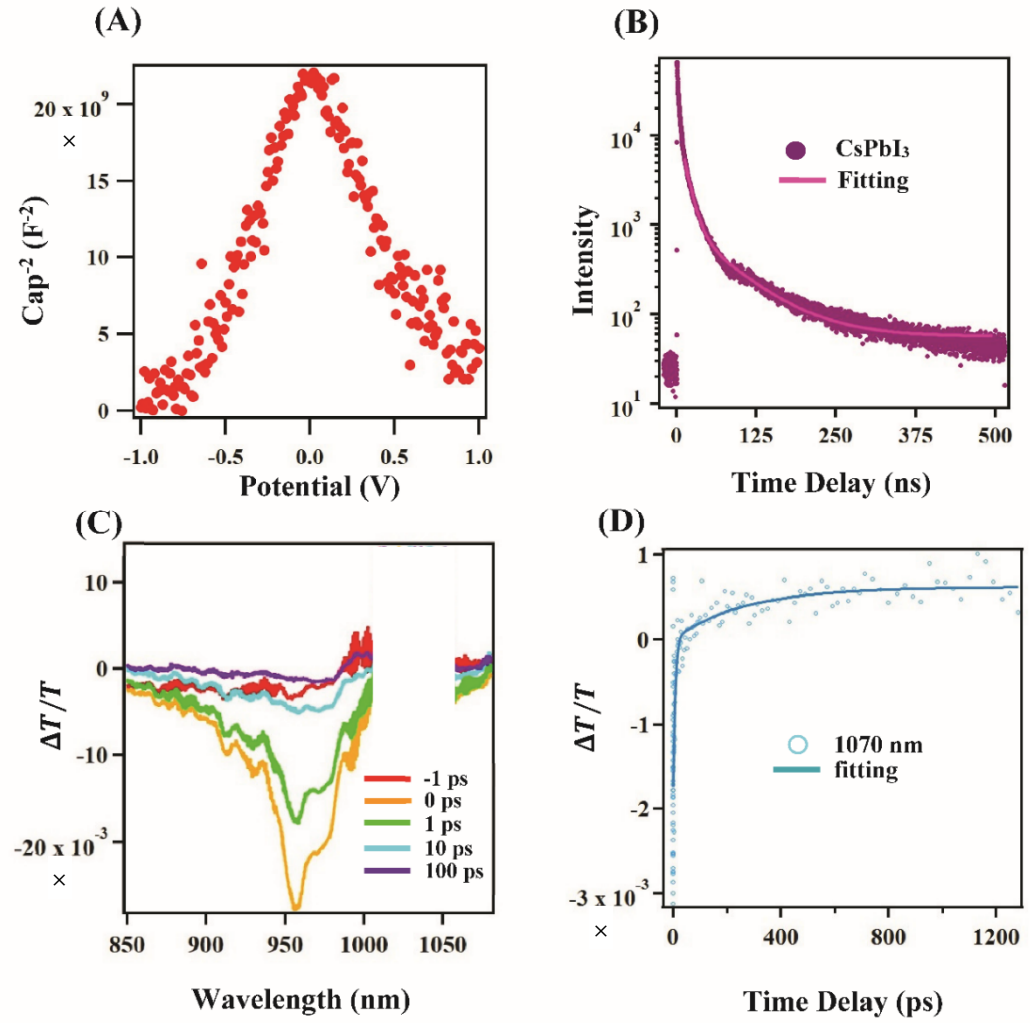


**Figure 3.** (**A**) Mott-Schottky plot of the fabricated all-inorganic perovskite photodetector; (**B**) Fluorescence lifetime measurements; (**C**) Transient absorption spectra of the PPD device at representative time delays; (**D**) Time traces of the TA response at 1070 nm.

**Table 1.** Comparison of representative SWIR detector performance based on material and operating parameters.

| Material | Light Source (nm) | Bias (V) | Responsivity (A/W) | Temperature (K) | Reference |
|---|---|---|---|---|---|
| $CsPbI_3$/HAI | 1310 | −5 | 1650 | Room temp. | This work |
| $[(MAI)_{0.835}(HAI)_{0.165}]_n[PbI_2]_1$ | 1310 | −5 | 157 | Room temp. | [41] |
| InAs/GaAs QDs | 2000 | −3 | 60.34 | 13 | [58] |
| Graphene/InGaAs | 1550 | 0–4 | 7.6 | Room temp. | [57] |
| $InAs/InAs_{1-x}Sb_x/AlAs_{1-x}Sb_x$ | 1600 | 0 | 0.47 | 300 | [7] |
| Graphene/black phosphorous | 1550 | 1 | 3300 | Room temp | [59] |
| Monolithic InSb | 1550 | 1 | 0.50 | 77 | [56] |

By doping all-inorganic $CsPbI_3$ perovskite with HAI, we have extended the useful range of such photodetectors into the SWIR region through engineering a *p-n* heterojunction between the doped and undoped materials. With the introduction of this heterojunction, the effective bandgap of $CsPbI_3$ is lowered to less than 1.0 eV, which allows for response to light in the SWIR region, where perovskites have historically been blind. Our PPD achieved moderate specific detectivity, very high gain and EQE, and an excellent responsivity of $1.65 \times 10^3$ A $W^{-1}$ at 1310 nm. A key feature of these PPDs is their ability to convert weak SWIR light to large amounts of current in ambient conditions without the need for cryogenic cooling systems. This makes our PPD especially appealing for integration into electronic systems, including low-light contexts like night vision and weather-impaired imaging, while decreasing cost and complexity.

While our $CsPbI_3$-HAI perovskite material shows potential in SWIR detection, improvements to the proof-of-concept device need to be made. One difficulty is that the absorption spectrum of the PPD was very affected by

small changes in fabrication conditions. Additionally, our experiments were implemented under ambient conditions, which resulted in poor stability, as shown in Figure S6 where the device's performance decreased over 80% in 6 days. This is most likely due to moisture and is typical for $CsPbI_3$ and other perovskites [37,52,58–60]. However, this can likely be remedied by mounting the device in a dedicated housing to ensure dry and nonreactive conditions during preparation and use as shown in the literature [61,62]. Lastly, being a Pb-containing material poses human and environmental health concerns. Proper handling and disposal must be considered if commercialization is to occur.

## 4. Conclusions

In summary, we produced all-inorganic SWIR materials using HAI as an additive to $CsPbI_3$ perovskite to engineer a *p-n* heterojunction within the material. We further developed simple and highly effective SWIR detectors based on the HAI-doped $CsPbI_3$ on a polymer HTL. We achieved a responsivity as high as $1.65 \times 10^3$ A $W^{-1}$ under 1310 nm light and −5 V bias at room temperature under fluence of 0.28 mW $cm^{-2}$. The detector also displayed an ultra-high EQE of $1.48 \times 10^3$ and gain of $1.42 \times 10^3$ under −5 V, exemplifying its strong ability to convert incoming photons to charge carriers supplied to the external circuit, which is essential for real-world application. Additionally, a specific detectivity of $8.0 \times 10^{10}$ Jones was found, demonstrating the sensitivity of this material. Our mechanistic studies show that a *p-n* junction was formed within the perovskite material between the doped and undoped phases. Fluorescence measurements characterized the carrier lifetimes in the material and TA revealed ultrafast charge transfer across the heterojunction. The performance of this material shows the potential for a new era of all-inorganic SWIR photodetectors which do not require extreme temperatures and conditions to achieve high performance, leading to important technological improvements without prohibitive costs.

**Supplementary Materials:** The following supporting information can be downloaded at: https://media.sciltp.com/articles/others/250730105027922 8/07-18-2025-all-inorganic-SI_Yi.pdf, Figure S1: Schematic of CsPbI3 device coating process. The main steps are preparation for PEDOT coating, PEDOT coating process, preparation for sample, and the sample coating process; Figure S2: XRD spectrum of $CsPbI_3$ material with HAI and 40 μL HI/mL; Figure S3: Absorption spectrum of prepared $CsPbI_3$ device.; Figure S4: Dark current at room temperature under a bias of −1 V (A) and −5 V (B); Figure S5: 2D plot of transient absorption spectra of the $CsPbI_3$ device with a time window of 10 ps (A) and 150 ps (B).; Figure S6: Normalized responsivity of the device over several days. Table S1: Photocurrent under 0.283 mW/cm2 illumination and corresponding gain separated by bias; Table S2: Specific detectivity at various bias if we assume $1 + 4\pi^2 f^2 \tau^2 = 1$.

**Author Contributions:** Y.R., G.C. and A.H. designed the project. S.S., H.F., X.L., Y.Q. and V.M. conducted experiments on material preparation, device fabrication, characterizations, analyzed the data. S.S., H.F. and J.B.B. drafted the manuscript. Y.R. and G.C. analyzed the data and revised the paper. All authors have read and agreed to the published version of the manuscript.

**Funding:** This research was funded by from Honda Research Institute USA, Inc. and the National Science Foundation, grant number 2045084.

**Data Availability Statement:** The datasets generated and/or analyzed during the current study are available from the corresponding authors on reasonable request.

**Conflicts of Interest:** The authors declare no conflict of interest.

## References

1. Cao, F.; Liu, L.; Li, L. Short-wave infrared photodetector. *Mater. Today* **2023**, *62*, 327–349. https://doi.org/10.1016/j.mattod.2022.11.003.
2. Wu, Z.; Zhai, Y.; Kim, H.; Azoulay, J.D.; Ng, T.N. Emerging Design and Characterization Guidelines for Polymer-Based Infrared Photodetectors. *Acc. Chem. Res.* **2018**, *51*, 3144–3153. https://doi.org/10.1021/acs.accounts.8b00446.
3. Saparbaev, A.; Zhang, M.; Kuvondikov, V.; Nurumbetova, L.; Raji, I.O.; Tajibaev, I.; Yang, R. High-performance CsPbI3 perovskite solar cells without additives in air condition. *Sol. Energy* **2021**, *228*, 405–412. https://doi.org/10.1016/j.solener.2021.09.059.
4. Shimoni, M.; Haelterman, R.; Perneel, C. Hypersectral Imaging for Military and Security Applications: Combining Myriad Processing and Sensing Techniques. *IEEE Geosci. Remote Sens. Mag.* **2019**, *7*, 101–117. https://doi.org/10.1109/MGRS.2019.2902525.
5. Liu, C.; Igci, C.; Yang, Y.; Syzgantseva, O.A.; Syzgantseva, M.A.; Rakstys, K.; Nazeeruddin, M.K. Dopant-Free Hole Transport Materials Afford Efficient and Stable Inorganic Perovskite Solar Cells and Modules. *Angew. Chem. Int. Ed.* **2021**, *60*, 20489–20497. https://doi.org/10.1002/anie.202107774.
6. Jahid, A.; Alsharif, M.H.; Hall, T.J. A contemporary survey on free space optical communication: Potentials, technical challenges, recent advances and research direction. *J. Netw. Comput. Appl.* **2022**, *200*, 103311. https://doi.org/10.1016/j.jnca.2021.103311.

7. Haddadi, A.; Suo, X.V.; Adhikary, S.; Dianat, P.; Chevallier, R.; Hoang, A.M.; Razeghi, M. High-performance short-wavelength infrared photodetectors based on type-II InAs/$InAs_{1-x}Sb_x$/$AlAs_{1-x}Sb_x$ superlattices. *Appl. Phys. Lett.* **2015**, *107*, 141104. https://doi.org/10.1063/1.4932518.
8. Richter, J.; Lorenz, S.; Kaas, A.; Fuchs, M.; Röder, C.; Peuker, U.A.; Gloaguen, R. Spectral Characterization of Battery Components from Li-Ion Battery Recycling Processes. *Metals* **2024**, *14*, 147.
9. Ferreira, M.P.; Wagner, F.H.; Aragão, L.E.O.C.; Shimabukuro, Y.E.; de Souza Filho, C.R. Tree species classification in tropical forests using visible to shortwave infrared WorldView-3 images and texture analysis. *ISPRS J. Photogramm. Remote Sens.* **2019**, *149*, 119–131. https://doi.org/10.1016/j.isprsjprs.2019.01.019.
10. Tan, C.L.; Mohseni, H. Emerging technologies for high performance infrared detectors. *Nanophotonics* **2018**, *7*, 169–197. https://doi.org/10.1515/nanoph-2017-0061.
11. Liu, Z.; Luo, T.; Liang, B.; Chen, G.; Yu, G.; Xie, X.; Shen, G. High-detectivity InAs nanowire photodetectors with spectral response from ultraviolet to near-infrared. *Nano Res.* **2013**, *6*, 775–783. https://doi.org/10.1007/s12274-013-0356-0.
12. Pokharel, R.; Ramaswamy, P.; Devkota, S.; Parakh, M.; Dawkins, K.; Penn, A.; Iyer, S. Epitaxial High-Yield Intrinsic and Te-Doped Dilute Nitride GaAsSbN Nanowire Heterostructure and Ensemble Photodetector Application. *ACS Appl. Electron. Mater.* **2020**, *2*, 2730–2738. https://doi.org/10.1021/acsaelm.0c00450.
13. Zhang, F.; Zhang, X.; Li, Z.; Yi, R.; Li, Z.; Wang, N.; Fu, L. A New Strategy for Selective Area Growth of Highly Uniform InGaAs/InP Multiple Quantum Well Nanowire Arrays for Optoelectronic Device Applications. *Adv. Funct. Mater.* **2022**, *32*, 2103057. https://doi.org/10.1002/adfm.202103057.
14. Ackerman, M.M. Bringing Colloidal Quantum Dots to Detector Technologies. *Inf. Disp.* **2020**, *36*, 19–23. https://doi.org/10.1002/msid.1165.
15. Wang, Y.; Peng, L.; Schreier, J.; Bi, Y.; Black, A.; Malla, A.; Konstantatos, G. Silver telluride colloidal quantum dot infrared photodetectors and image sensors. *Nat. Photonics* **2024**, 18, 236–242. https://doi.org/10.1038/s41566-023-01345-3.
16. Wu, Z.; Ou, Y.; Cai, M.; Wang, Y.; Tang, R.; Xia, Y. Short-Wave Infrared Photodetectors and Imaging Sensors Based on Lead Chalcogenide Colloidal Quantum Dots. *Adv. Opt. Mater.* **2023**, *11*, 2201577. https://doi.org/10.1002/adom.202201577.
17. Kwon, J.B.; Han, M.; Jung, D.G.; Kong, S.H.; Jung, D. High Sensitivity Shortwave Infrared Photodetector Based on PbS QDs Using P3HT. *Nanomaterials* **2021**, *11*, 2683.
18. Chen, W.; Tang, H.; Chen, Y.; Heger, J.E.; Li, N.; Kreuzer, L.P.; Müller-Buschbaum, P. Spray-deposited PbS colloidal quantum dot solid for near-infrared photodetectors. *Nano Energy* **2020**, *78*, 105254. https://doi.org/10.1016/j.nanoen.2020.105254.
19. Yu, M.X.; Ma, J.J.; Wang, J.M.; Cai, W.G.; Zhang, Z.; Huang, B.; Tian, Z.Q. $Ag_2Te$ Quantum Dots as Contrast Agents for Near-Infrared Fluorescence and Computed Tomography Imaging. *ACS Appl. Nano Mater.* **2020**, *3*, 6071–6077. https://doi.org/10.1021/acsanm.0c01274.
20. Hu, L.; Dong, Y.; Deng, J.; Xie, Y.; Ma, X.; Qian, F.; Xu, C. High responsivity graphene-InGaAs near-infrared photodetector realized by hole trapping and its response saturation mechanism. *Opt. Express* **2021**, *29*, 23234–23243. https://doi.org/10.1364/OE.431083.
21. Park, J.; Hwang, J.C.; Kim, G.G.; Park, J.-U. Flexible electronics based on one-dimensional and two-dimensional hybrid nanomaterials. *InfoMat* **2020**, *2*, 33–56. https://doi.org/10.1002/inf2.12047.
22. Mak, K.F.; Ju, L.; Wang, F.; Heinz, T.F. Optical spectroscopy of graphene: From the far infrared to the ultraviolet. *Solid State Commun.* **2012**, *152*, 1341–1349. https://doi.org/10.1016/j.ssc.2012.04.064.
23. Kim, J.Y.; Lee, J.-W.; Jung, H.S.; Shin, H.; Park, N.-G. High-Efficiency Perovskite Solar Cells. *Chem. Rev.* **2020**, *120*, 7867–7918. https://doi.org/10.1021/acs.chemrev.0c00107.
24. Gao, W.-H.; Chen, C. Perovskites and their constructed near-infrared photodetectors. *Nano Energy* **2024**, *128*, 109904. https://doi.org/10.1016/j.nanoen.2024.109904.
25. Jhang, A.-T.; Tsai, P.-C.; Tsai, Y.-T.; Lin, S.-Y.; Fang, M.-H. Quantum-Dots-In-Double-Perovskite for High-Gain Short-Wave Infrared Photodetector. *Adv. Opt. Mater.* **2024**, *12*, 2401252. https://doi.org/10.1002/adom.202401252.
26. Qian, Y.; Huang-Fu, Z.C.; Li, H.; Zhang, T.; Li, X.; Schmidt, S.; Rao, Y. Unleashing the Potential: High Responsivity at Room Temperature of Halide Perovskite-Based Short-Wave Infrared Detectors with Ultrabroad Bandwidth. *JACS Au* **2024**, 4, 3921–3930. https://doi.org/10.1021/jacsau.4c00621.
27. Wang, H.; Sun, Y.; Chen, J.; Wang, F.; Han, R.; Zhang, C.; Yang, J. A Review of Perovskite-Based Photodetectors and Their Applications. *Nanomaterials* **2022**, *12*, 4390.
28. Miao, J.; Zhang, F. Recent progress on highly sensitive perovskite photodetectors. *J. Mater. Chem. C* **2019**, *7*, 1741–1791. https://doi.org/10.1039/C8TC06089D.
29. Wang, F.; Zou, X.; Xu, M.; Wang, H.; Wang, H.; Guo, H.; Hu, W. Recent Progress on Electrical and Optical Manipulations of Perovskite Photodetectors. *Adv. Sci.* **2021**, *8*, 2100569. https://doi.org/10.1002/advs.202100569.
30. Li, L.; Ye, S.; Qu, J.; Zhou, F.; Song, J.; Shen, G. Recent Advances in Perovskite Photodetectors for Image Sensing. *Small* **2021**, *17*, 2005606. https://doi.org/10.1002/smll.202005606.

31. Fakharuddin, A.; Gangishetty, M.K.; Abdi-Jalebi, M.; Chin, S.H.; bin Mohd Yusoff, A.R.; Congreve, D.N.; Bolink, H.J. Perovskite light-emitting diodes. *Nat. Electron.* **2022**, *5*, 203–216. https://doi.org/10.1038/s41928-022-00745-7.
32. Liu, Y.; Xia, M.; Ren, D.; Nussbaum, S.; Yum, J.H.; Gratzel, M.; Sivula, K. Photoelectrochemical $CO_2$ Reduction at a Direct CuInGaS2/Electrolyte Junction. *ACS Energy Lett.* **2023**, *8*, 1645–1651. https://doi.org/10.1021/acsenergylett.3c00022.
33. Filip, M.R.; Eperon, G.E.; Snaith, H.J.; Giustino, F. Steric engineering of metal-halide perovskites with tunable optical band gaps. *Nat. Commun.* **2014**, *5*, 5757. https://doi.org/10.1038/ncomms6757.
34. Chen, S.; Teng, C.; Zhang, M.; Li, Y.; Xie, D.; Shi, G. A Flexible UV–Vis–NIR Photodetector based on a Perovskite/Conjugated-Polymer Composite. *Adv. Mater.* **2016**, *28*, 5969–5974. https://doi.org/10.1002/adma.201600468.
35. Alwadai, N.; Haque, M.A.; Mitra, S.; Flemban, T.; Pak, Y.; Wu, T.; Roqan, I. High-Performance Ultraviolet-to-Infrared Broadband Perovskite Photodetectors Achieved via Inter-/Intraband Transitions. *ACS Appl Mater Interfaces* **2017**, *9*, 37832–37838. https://doi.org/10.1021/acsami.7b09705 From NLM.
36. Pan, X.; Zhou, H.; Liu, R.; Wu, D.; Song, Z.; Tang, X.; Wang, H. Achieving a high-performance, self-powered, broadband perovskite photodetector employing MAPbI3 microcrystal films. *J. Mater. Chem. C* **2020**, *8*, 2028–2035. https://doi.org/10.1039/C9TC05668H.
37. Yao, Z.; Zhao, W.; Liu, S. Stability of the $CsPbI_3$ perovskite: From fundamentals to improvements. *J. Mater. Chem. A* **2021**, *9*, 11124–11144. https://doi.org/10.1039/D1TA01252E.
38. Li, Y.; Shi, Z.; Lei, L.; Zhang, F.; Ma, Z.; Wu, D.; Li, X. Highly Stable Perovskite Photodetector Based on Vapor-Processed Micrometer-Scale CsPbBr3 Microplatelets. *Chem. Mater.* **2018**, *30*, 6744–6755. https://doi.org/10.1021/acs.chemmater.8b02435.
39. Pintor Monroy, M.I.; Goldberg, I.; Elkhouly, K.; Georgitzikis, E.; Clinckemalie, L.; Croes, G.; Genoe, J. All-Evaporated, All-Inorganic $CsPbI_3$ Perovskite-Based Devices for Broad-Band Photodetector and Solar Cell Applications. *ACS Appl. Electron. Mater.* **2021**, *3*, 3023–3033. https://doi.org/10.1021/acsaelm.1c00252.
40. Liu, X.; Liu, Z.; Li, J.; Tan, X.; Sun, B.; Fang, H.; Liao, G. Ultrafast, self-powered and charge-transport-layer-free photodetectors based on high-quality evaporated $CsPbBr_3$ perovskites for applications in optical communication. *J. Mater. Chem. C* **2020**, *8*, 3337–3350. https://doi.org/10.1039/C9TC06630F.
41. Han, J.; Xie, Q.; Luo, J.; Deng, G.H.; Qian, Y.; Sun, D.; Rao, Y. Anisotropic Geminate and Non-Geminate Recombination of Triplet Excitons in Singlet Fission of Single Crystalline Hexacene. *J. Phys. Chem. Lett.* **2020**, *11*, 1261–1267. https://doi.org/10.1021/acs.jpclett.9b03800.
42. Haque, F.; Wright, M.; Mahmud, M.A.; Yi, H.; Wang, D.; Duan, L.; Uddin, A. Effects of Hydroiodic Acid Concentration on the Properties of CsPbI 3 Perovskite Solar Cells. *ACS Omega* **2018**, *3*, 11937–11944. https://doi.org/10.1021/acsomega.8b01589.
43. Ke, F.; Wang, C.; Jia, C.; Wolf, N.R.; Yan, J.; Niu, S.; Lin, Y. Preserving a robust $CsPbI_3$ perovskite phase via pressure-directed octahedral tilt. *Nat. Commun.* **2021**, *12*, 461. https://doi.org/10.1038/s41467-020-20745-5.
44. Luo, P.; Xia, W.; Zhou, S.; Sun, L.; Cheng, J.; Xu, C.; Lu, Y. Solvent Engineering for Ambient-Air-Processed, Phase-Stable CsPbI3 in Perovskite Solar Cells. *J. Phys. Chem. Lett.* **2016**, *7*, 3603–3608. https://doi.org/10.1021/acs.jpclett.6b01576.
45. Montecucco, R.; Quadrivi, E.; Po, R.; Grancini, G. All-Inorganic Cesium-Based Hybrid Perovskites for Efficient and Stable Solar Cells and Modules. *Adv. Energy Mater.* **2021**, *11*, 2100672. https://doi.org/10.1002/aenm.202100672.
46. Liu, D.; Li, Y.; Yuan, J.; Hong, Q.; Shi, G.; Yuan, D.; Fung, M.K. Improved performance of inverted planar perovskite solar cells with F4-TCNQ doped PEDOT:PSS hole transport layers. *J. Mater. Chem. A* **2017**, *5*, 5701–5708. https://doi.org/10.1039/C6TA10212C.
47. Yan, G.; Ji, Z.; Li, Z.; Jiang, B.; Kuang, M.; Cai, X.; Mai, W. All-inorganic $Cs_2AgBiBr_6$/CuSCN-based photodetectors for weak light imaging. *Sci. China Mater.* **2021**, *64*, 198–208. https://doi.org/10.1007/s40843-020-1358-5.
48. Wang, F.; Zhang, T.; Xie, R.; Wang, Z.; Hu, W. How to characterize figures of merit of two-dimensional photodetectors. *Nat. Commun.* **2023**, *14*, 2224. https://doi.org/10.1038/s41467-023-37635-1.
49. Naeem, R.; Ehsan, M.; Rehman, A.; Yamani, Z.; Hakeem, A.; Mazhar, M. Single step aerosol assisted chemical vapor deposition of p-n Sn(II)oxide-Ti(IV)oxide nanocomposite thin film electrodes for investigation of photoelectrochemical properties. *N. J. Chem.* **2018**, *42*, 5256–5266. https://doi.org/10.1039/C7NJ04606E.
50. Zhang, L.; Zhou, M.; Zhang, Z.; Yuan, J.; Li, B.; Wen, W.; Tian, J. Ultra-long photoluminescence lifetime in an inorganic halide perovskite thin film. *J. Mater. Chem. A* **2019**, *7*, 22229–22234. https://doi.org/10.1039/C9TA07412K.
51. Zhang, Z.; Ji, R.; Kroll, M.; Hofstetter, Y.J.; Jia, X.; Becker-Koch, D.; Vaynzof, Y. Efficient Thermally Evaporated γ-$CsPbI_3$ Perovskite Solar Cells. *Adv. Energy Mater.* **2021**, *11*, 2100299. https://doi.org/10.1002/aenm.202100299.
52. Fu, Y.; Rea, M.T.; Chen, J.; Morrow, D.J.; Hautzinger, M.P.; Zhao, Y.; Jin, S. Selective Stabilization and Photophysical Properties of Metastable Perovskite Polymorphs of $CsPbI_3$ in Thin Films. *Chem. Mater.* **2017**, *29*, 8385–8394. https://doi.org/10.1021/acs.chemmater.7b02948.
53. You, J.; Hong, Z.; Yang, Y.; Chen, Q.; Cai, M.; Song, T.B.; Yang, Y. Low-Temperature Solution-Processed Perovskite Solar Cells with High Efficiency and Flexibility. *ACS Nano* **2014**, *8*, 1674–1680. https://doi.org/10.1021/nn406020d.
54. Menon, H.; Jeddi, H.; Morgan, N.P.; Fontcuberta i Morral, A.; Pettersson, H.; Borg, M. Monolithic InSb nanostructure photodetectors on Si using rapid melt growth. *Nanoscale Adv.* **2023**, *5*, 1152–1162. https://doi.org/10.1039/D2NA00903J.

55. Yang, Q.; Wu, Q.; Luo, W.; Yao, W.; Yan, S.; Shen, J. InGaAs/graphene infrared photodetectors with enhanced responsivity. *Mater. Res. Express* **2019**, *6*, 116208. https://doi.org/10.1088/2053-1591/ab4925.
56. Deviprasad, V.P.; Ghadi, H.; Das, D.; Panda, D.; Rawool, H.; Chavan, V.; Chakrabarti, S. High performance short wave infrared photodetector using p-i-p quantum dots (InAs/GaAs) validated with theoretically simulated model. *J. Alloys Compd.* **2019**, *804*, 18–26. https://doi.org/10.1016/j.jallcom.2019.06.286.
57. Liu, Y.; Shivananju, B.N.; Wang, Y.; Zhang, Y.; Yu, W.; Xiao, S.; Bao, Q. Highly Efficient and Air-Stable Infrared Photodetector Based on 2D Layered Graphene–Black Phosphorus Heterostructure. *ACS Appl. Mater. Interfaces* **2017**, *9*, 36137–36145. https://doi.org/10.1021/acsami.7b09889.
58. Ouedraogo, N.A.N.; Chen, Y.; Xiao, Y.Y.; Meng, Q.; Han, C.B.; Yan, H.; Zhang, Y. Stability of all-inorganic perovskite solar cells. *Nano Energy* **2020**, *67*, 104249. https://doi.org/10.1016/j.nanoen.2019.104249.
59. Wang, D.; Wright, M.; Elumalai, N.K.; Uddin, A. Stability of perovskite solar cells. *Sol. Energy Mater. Sol. Cells* **2016**, *147*, 255–275. https://doi.org/10.1016/j.solmat.2015.12.025.
60. Boyd, C.C.; Cheacharoen, R.; Leijtens, T.; McGehee, M.D. Understanding Degradation Mechanisms and Improving Stability of Perovskite Photovoltaics. *Chem. Rev.* **2019**, *119*, 3418–3451. https://doi.org/10.1021/acs.chemrev.8b00336.
61. Wang, P.; Zhang, X.; Zhou, Y.; Jiang, Q.; Ye, Q.; Chu, Z.; You, J. Solvent-controlled growth of inorganic perovskite films in dry environment for efficient and stable solar cells. *Nat. Commun.* **2018**, *9*, 2225. https://doi.org/10.1038/s41467-018-04636-4.
62. Bian, H.; Bai, D.; Jin, Z.; Wang, K.; Liang, L.; Wang, H.; Liu, S.F. Graded Bandgap $CsPbI_2$+x$Br_{1-x}$ Perovskite Solar Cells with a Stabilized Efficiency of 14.4%. *Joule* **2018**, *2*, 1500–1510. https://doi.org/10.1016/j.joule.2018.04.012.